ADVANCED FUNCTIONAL MATERIALS
www.afm-journal.de

Low-Temperature Sodium–Sulfur Batteries Enabled by Ionic Liquid in Localized High Concentration Electrolytes

Dong Guo, Jiaao Wang, Zehao Cui, Zixiong Shi, Graeme Henkelman, Husam N. Alshareef, and Arumugam Manthiram**

Low ionic migration and compromised interfacial stability pose challenges for low-temperature batteries. In this work, we discovered that even with the state-of-the-art localized high-concentration electrolytes (LHCEs), uncontrolled Na electrodeposition occurs with a huge overpotential of >1.2 V at −20 °C, leading to cell failure within tens of hours. To address this, we introduce a new electrolyte category that incorporates an ionic liquid as a key solvation species. Diverging from traditional LHCEs, the IL-tailored LHCE facilitates an anion–solvent-molecules exchange within the solvation sheath between Na^+ and organic cations at low temperatures. This behavior reduces solvation cluster size and strengthens Na^+–anion coordination, which proves instrumental in enabling fast ionic dynamics in both the bulk liquid and at the interface. Therefore, durable Na electrodeposition and shuttle-free, 0.5 Ah sodium–sulfur pouch cells are achieved at −20 °C, for the first time, surpassing the limitations of typical LHCEs. This tailoring strategy opens a new design direction for advanced batteries operating in fast-charge and wide-temperature scenarios.

1. Introduction

Lithium–sulfur (Li–S) batteries have been intensively investigated due to the low cost and high theoretical capacity (1675 mA h g^{-1}) of sulfur.[1–5] However, considering the much greater earth-abundance of sodium (2.3 wt.%) compared to lithium (0.0017 wt.%) and its global availability, room temperature (RT) sodium–sulfur (Na–S) batteries present a more sustainable option for grid-level energy storage.[2,6,7] The RT Na–S batteries offer a theoretical energy density of 1274 Wh kg^{-1}, with sodium raw material cost less than 10% of that of lithium. Nevertheless, the RT Na–S remains in its early stage and faces more paramount challenges than its Li–S counterparts. These challenges fundamentally result from the lack of suitable electrolytes that can stabilize both the highly reactive sodium-metal anodes and the soluble sulfur cathodes.[8]

Regulating electrolyte solvation structure is a key strategy for harnessing highly reactive, yet energy-dense anodes as it dictates both bulk electrolyte properties and electrical interface.[9–19] Ether-based electrolytes with $NaPF_6$ salt have demonstrated high-quality Na deposition even at low temperatures,[20,21] but they are not suitable in Na–S batteries. This is because the relatively low solubility of $NaPF_6$ in ether brings substantial free solvents (even weakly solvating solvents), thereby causing serious sulfur species dissolution and rapid capacity loss, which is a much more exacerbated issue in Na–S batteries than in Li–S.[22–28] Localized high-concentration electrolytes (LHCE) are promising in stabilizing metal anodes.[29–32] The cation-anion aggregates in LHCE preferentially induce anion reduction to form an inorganic-rich solid electrolyte interface (SEI), which reduces the parasite reactions of solvents at interphase. More importantly, the LHCEs with much less free solvents can suppress the cathode dissolution. Nevertheless, the current LHCE formulations fall short, particularly in low-temperature and high-rate cycling scenarios. Although an inert non-solvating diluent is added in LHCEs to offer a lower viscosity, the large coordination clusters still hinder the ion migration and de-solvation at sub-zero temperatures, leading to surged cell impedance and capacity deterioration.[33–38] Previous strategies for low-temperature electrolytes have primarily focused on weakly solvating electrolytes (WSE) using fluorinated solvents.[21,39,40] This is because the anion-derived inorganic SEI formed in WSE is favorable for interfacial kinetics at low temperatures. However, these strategies have generally been successful in lithium-ion batteries, but have shown limited effectiveness in Na–S batteries due to the extremely high solubility of sodium polysulfides and the high reactivity of sodium-metal anode. More importantly, how the Na^+-anion/solvent coordination behavior, ionic transport, and SEI formation transform in low-temperature LHCEs remains ambiguous. For example, even with the

D. Guo, Z. Cui, A. Manthiram
Materials Science and Engineering Program and Texas Materials Institute
The University of Texas at Austin
Austin, TX 78712, USA
E-mail: manth@austin.utexas.edu
J. Wang, G. Henkelman
Department of Chemistry
The University of Texas at Austin
Austin, TX 78712, USA
Z. Shi, H. N. Alshareef
Materials Science and Engineering
Physical Science and Engineering Division
King Abdullah University of Science and Technology (KAUST)
Thuwal 23955–6900, Saudi Arabia
E-mail: husam.alshareef@kaust.edu.sa
The ORCID identification number(s) for the author(s) of this article can be found under https://doi.org/10.1002/adfm.202409494

DOI: 10.1002/adfm.202409494

state-of-the-art LHCEs, we find that the SEI formed at −20 °C is composed of organic-rich components instead of the usually observed inorganic-dominated components at room temperature. In this context, the conventional LHCEs should be redesigned, especially for low-temperature conditions.

In this work, by using an ionic liquid (IL) *N*-Propyl, *N*-methyl pyrrolidinium bis(fluorosulfonyl)imide (C_3mpyrFSI) as a model additive, a new type of LHCE is presented for Na–S batteries working at low temperatures. While ILs are generally used in room/high-temperature batteries due to low volatility and nonflammability, their solvation structures and application at low temperatures are largely unexplored. Moreover, although IL-salt binary systems or even localized high-concentration ILs have been proposed for lithium batteries,[41,42] we find that they do not work with sodium anode (Figure S1, Supporting Information). Actually, the strong cation−anion interactions in the IL-salt system lead to the formation of negatively charged $[Na^+(anion)_n]^{-(n-1)}$ clusters, which force the cation to migrate toward the positively charged electrode and thus into the "wrong" direction ($t^+ < 0$).[43–44] This in return can cause high polarization (>3 V) and failure of sodium deposition (Figure S1, Supporting Information). In contrast, we found that by supplementing the LHCE with a proper amount of C_3mpyrFSI, the IL acts as a special diluent in the solution, which not only increases ionic mobility by developing smaller solvation cluster size (illustrated in Figure S2, Supporting Information) but also reconstructs microstructure by anion-solvent exchange within Na^+ and organic cations. Additionally, a more compact and durable SEI layer is formed on the sodium-metal anode, regardless of the temperature-dependent Na deposition behavior. Therefore, with sulfurized polyacrylonitrile (SPAN) as the cathode, Na–S pouch cells with remarkably high Coulombic efficiencies (CEs) (>99.8%) and sulfur utilization are achieved at −20 °C. This study represents the first investigation of low-temperature Na–S batteries and sheds light on the role of ionic liquid in low-temperature electrolytes.

2. Results and Discussion

While LHCE is efficient in improving the alkali-metal deposition quality, we found that the Na deposition is much more sensitive to the molar ratio of salt/solvent in LHCE. For example, in a typical LHCE of sodium bis(fluoro sulfonyl)imide (NaFSI): Dimethoxyethane (DME): 1,1,2,2-Tetrafluoroethyl 2,2,3,3-tetrafluoropropyl ether (TTE) with a molar ratio 1:1.3:1, the Cu | Na cell exhibits a high CE of ≈97.5% at 20 °C (**Figure 1a**), which outperforms LHCE with a ratio of 1:1.5:1 (≈96.2%, Figure S3, Supporting Information). This difference emphasizes the importance of eliminating free solvents in LHCEs to modulate the Na anode. Nevertheless, reducing the amount of DME solvent further to form a 1:1.1:1 LHCE caused phase separation once a small amount of DME evaporates during cell assembly, which causes the risk of cell failure. In contrast, when a certain amount of C_3mpyrFSI was introduced to form an IL-based LHCE_X (X refers to the molar ratio of ionic liquid), the Cu | Na cell exhibited a greatly improved CE without the risk of salt-out. Here, the LHCE_0.3IL, formulated with a NaFSI:DME:TTE:C_3mpyrFSI ratio of 1:1.3:1:0.3, has a CE of ≈99.1% after 500 cycles at 20 °C (Figure 1a). More importantly, kinetic enhancement is much more prominent at a low temperature. As plotted in Figure 1b, the Na^+ deposition at −20 °C in the LHCE (1:1.3:1) exhibited a huge overpotential of 1.2 V at a current density of 0.1 mA cm^{-2}, while this overpotential is greatly reduced to ≈200 mV in the LHCE_0.3IL electrolyte. To understand the mechanism behind this distinctive difference, the temperature-dependent ionic conductivities and viscosity were first measured.

Figure 1c shows that the ionic conductivity (σ) of LHCE_0.3IL is≈1.5–2 times of bare LHCE throughout the -20–20 °C (Figure S4, Supporting Information). Since the ionic liquid also contributes to the ionic conductivity of the LHCE_0.3IL electrolyte, the molar conductivity was also calculated and is summarized in Table S1 (Supporting Information). It was found that the molar conductivity of LHCE_0.3IL is still≈1.2–1.6 times of bare LHCE throughout the -20–20 °C temperature range. Nevertheless, the viscosity test showed that LHCE_0.3IL has a comparable or even slightly higher viscosity (Figure 1c). This means the viscosity effect cannot explain the enhanced ionic conductivity and deposition kinetics in IL-tailored LHCE. To this end, small angle X-ray scattering (SAXS), which is sensitive to clusters and networks formed in liquids, was utilized to provide insights into the mesoscopic properties. SAXS data in Figure 1e show that at scattering vector (Q) values of 1.3–1.7 $Å^{-1}$ (corresponding to 4.8–3.7 Å), all the electrolytes and baseline DME/TTE solvent exhibit a broad peak, which is typically related to short-range intra/inter-molecular distances in liquids. However, compared with pure solvent, LHCE exhibits additional scattering at a low Q value of 0.6 $Å^{-1}$, signifying the formation of long-range and large Na^+ solvation clusters with the size of 10.5 Å calculated by Bragg's law, $d = 2\pi\ Q^{-1}$. This phenomenon is also corroborated by concentration-dependent SAXS analysis (Figure S5, Supporting Information) and other scattering experiments in high-concentration electrolytes.[45,46] More importantly, once the IL is dissolved into LHCE, this scattering moves to a higher Q value (0.73 $Å^{-1}$), which means these large clusters in LHCE are developed into a smaller size (8.6 Å) in LHCE_0.3IL. Cluster size plays an important role in ionic mobility. According to Stokes-Einstein relation, $D = \frac{K_B T}{6\pi\eta R}$ diffusion coefficient (D) is inversely proportional to the hydrodynamic radius (R). Decreased cluster size means a smaller hydrodynamic radius. Therefore, the IL is more like a functional diluent that could break the large micelles/clusters of LHCE into smaller individual ones, which is the key factor to realize higher ionic migration under a similar viscosity (η) condition in LHCE_0.3IL. Increasing the IL ratio to 1:1:3: 1:0.5 (LHCE_0.5IL) slightly enhances the overall ionic conductivity (Figure S4, Supporting Information) but decreases the transference number (t_+) of the cation (Figures S6, S7, and Table S2, Supporting Information). This decrease occurs because an excess of IL causes the formation of negatively charged $[Na^+(anion)^n]^{-(n-1)}$ clusters, leading to vehicular transport by anionic clusters.[43] Conversely, LHCE_0.1IL showed only limited enhancement in ionic conductivity and delivered lower discharge capacities compared to LHCE_0.3IL (Figure S8, Supporting Information). Therefore, LHCE-0.3IL was selected as the target electrolyte for further investigation.

As well as considering the macroscopic properties and mesoscopic structure, the local solvation environment was

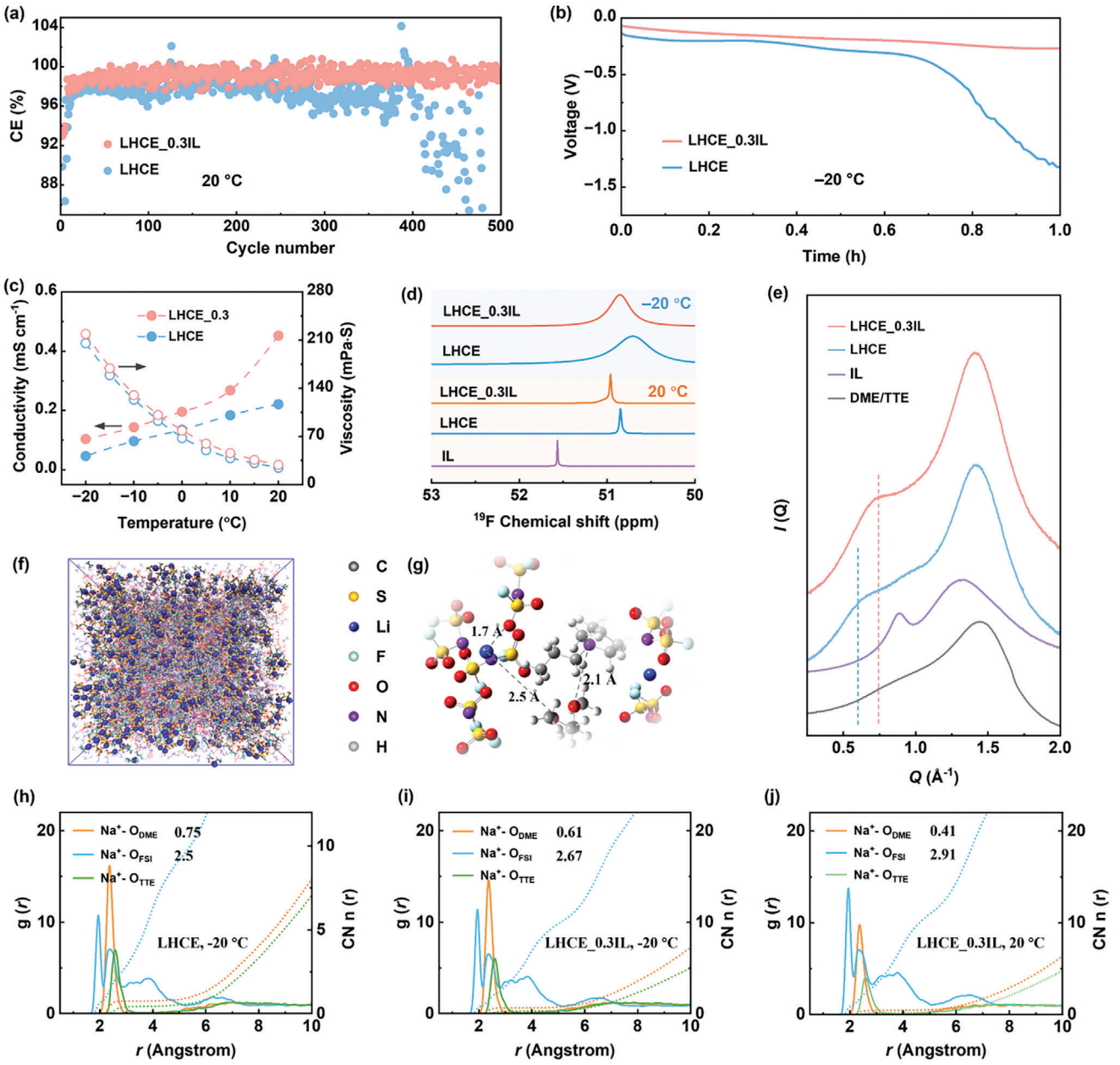

Figure 1. a) Na plating/stripping CE on a Cu electrode with electrolytes at 0.5 mA cm^2. b) Comparison of the overpotential of Na deposition at −20 °C at 0.1 mA cm^{-2} in Na | Na symmetric cell. c) Temperature-dependent viscosity and ionic conductivity of the electrolytes. d) ^{19}F NMR spectra of the electrolytes at 20 °C and −20 °C. e) SAXS profiles for the solvents and electrolytes. f) Snapshots of LHCE_0.3IL from MD simulation at −20 °C and g) the representative local solvation structure. h–j) The RDFs were derived from MD simulations for the electrolytes at 20 and −20 °C.

further investigated by nuclear magnetic resonance (NMR) spectroscopy. Compared with the ^{19}F NMR spectrum of FSI$^-$ in pure C_3mpyrFSI IL, an obvious upfield (negative) shifted signal is observed in bare LHCE at 20 °C (Figure 1d). The more negative chemical shift results from an increased electron density in FSI anions (shielded effect), indicating a weekended FSI$^-$···Na$^+$ coordination in LHCE compared with pure IL, which is understandable since the DME molecules in LHCE partially shield the Na$^+$···FSI$^-$ coordination. Once the ionic liquid is added to LHCE, the ^{19}F spectrum is more downfield-shifted (51 ppm) compared with that of bare LHCE (50.8 ppm). This means the IL plays a role in enhancing Na$^+$···FSI$^-$ coordination in LHCE_0.3IL. This conclusion is validated by the ^{23}Na NMR spectrum in Figure S9 (Supporting Information). The stronger Na$^+$···FSI$^-$ ionic pairing in LHCE_0.3IL intensifies electron density around Na$^+$, thus causing a more negative ^{23}Na chemical shift. More importantly, low-temperature NMR shows that ^{19}F signals are negatively shifted when the electrolytes are down to −20 °C, indicating weaker FSI$^-$···Na$^+$ pairs occur at a decreased temperature. Even so, the IL offered the traditional LHCE a relatively stable Na···FSI$^-$

coordination at a low temperature, as revealed by a more positive ^{19}F shift of FSI^- anion at −20 °C (Figure 1e). Moreover, in contrast to the negative ^{23}Na shift at 20 °C, the ^{23}Na chemical shift of LHCE-0.3IL is more positive than that of LHCE at −20 °C (Figure S10, Supporting Information). Note that a higher Na^+ chemical shift means less electron shield effect that arises from either a weaker ion solvation or a decreased ionic pairing. So, considering the stronger $Na^+\cdots FSI^-$ ion pairing in LHCE_03IL (revealed by ^{19}F NMR), the higher ^{23}Na chemical shift in LHCE_0.3IL must arise from a much weaker $Na^+\cdots$DME solvation at −20 °C, telling the fact that DME solvents tend to separate from Na^+. This fact is also confirmed by ^1H NMR in Figures S10 and S11 (Supporting Information). These weakened cation-solvent pairs and strengthened cation-anion ionic pairs are crucial to SEI structures at a low temperature as will be discussed later. By contrast, the lower chemical shift ^{19}F for traditional LHCE (Figure 1e) at −20 °C indicates the more temperature-sensitive Na-ion solvation and relatively weak $Na^+\cdots FSI^-$ pairs.

To further quantify how the IL mediates LHCE in terms of enhanced Na-anion interaction, molecular dynamic (MD) simulations at 20 and −20 °C were performed. The snapshoots and radial distribution functions (RDFs) (Figure 1f–j) present the typical solvation of LHCE featuring $Na^+\cdots FSI^-$ ion pair-dominated inner shell and TTE outer shell. LHCE_0.3IL exhibits a similar solvation behavior, but the time-averaged coordination number (CN) shows a discrepancy. The CN of LHCE is calculated to be 2.7 O_{FSI} and 0.63 O_{DME} per Na^+ in LHCE at 20 °C (Figure S12, Supporting Information), denoted as $Na^+(O_{FSI})_{2.7}(O_{DME})_{0.63}$. This solvation formula transformed to $Na^+(FSI)_{2.91}(O_{DME})_{0.41}$ for LHCE_0.3IL (Figure 1j), i.e., the C_3mpyrFSI facilitates more FSI anions entering Na^+ inner sheath while fewer DME coordinate with Na^+ cations. This spatial reconstruction is favorable since during Na deposition, the species' proximity to the Na^+ inner sheath is more likely to be dragged into the interphase and thereafter be preferentially reduced. In this case, the LHCE_0.3IL is more likely to enable an anion-derived SEI. The typical snapshoot of LHCE_0.3IL (Figure 1g) also shows a shorter distance (1.7 Å) between O_{FSI} and Na^+ than the bond length between O_{DME} and Na^+ (2.5 Å). At a lower temperature of −20 °C more solvents enter the Na^+ solvation sheath, as revealed by the transformed formula $Na^+(O_{FSI})_{2.5}(O_{DME})_{0.75}$ and $Na^+(O_{FSI})_{2.7}(O_{DME})_{0.62}$, respectively, for LHCE and LHCE-0.3IL (Figure 1h,i; Figure S13, Supporting Information). Nevertheless, the LHCE_0.3IL still possess more $Na^+\cdots FSI^-$ ion pairs (2.7) than LHCE in the primary shell at −20 °C (2.5), and the CN of undesired $Na^+\cdots$DME pair in LHCE_0.3IL at −20 °C is even as low as the bare LHCE at 20 °C. Therefore, instead of constructing super concentrated electrolytes by increasing solid salt content that causes low ionic conductivity and compromised solvation at low temperatures, we found that a proper amount of liquid IL could upgrade the meso-/micro-structures.

Considering the decreased CN of $Na^+\cdots FSI^-$ pairs in bare LHCE at lower temperatures, the increased $Na^+\cdots FSI^-$ pairs in LHCE_0.3IL (compared to LHCE) at −20 °C could only arise from the coupling of FSI^- from C_3mpyrFSI, while the decreased $Na^+\cdots$DME population may result from the competitive solvation of C_3mpyr with DME, which attracts the solvents from inorganic cations to the organic cations. This intermolecular arrangement was further deciphered by the nuclear Overhauser effect (NOE), which is a powerful tool to detect spatial coupling strength.[47] Nuclei that are in proximity within the NMR time scale give rise to off-diagonal (cross) peaks in 2D contour plots. As shown in 2D nuclear Overhauser effect spectroscopy (NOESY) in **Figure 2**a, LHCE_0.3IL at −20 °C exhibits clear ^1H-^1H off-diagonal peaks (indicated by dash lines), which arise from the coupling of the methylene/methyl protons in C_3mPyr cations with the protons in DME solvents. Notably, these NOEs at −20 °C are much stronger than those at 20 °C (Figure 2b), reflecting an enhanced $Pyr^+\cdots$DME solvation with a closer average distance of −20 °C. Meanwhile, the 2D ^1H-^{19}F heteronuclear Overhauser effect spectroscopy (HOESY) detected a much weaker cross-peak intensity between FSI anion (51 ppm) and methyl protons (0.9 ppm) of Pyr^+ cation at −20 °C than those at 20 °C, indicating the FSI^- anion tends to depart from organic cations at a lower temperature (Figure 2c,d). Hence, from the perspective of organic cations, adding liquid C_3mpyrFSI in bare LHCE tends to remove DME solvents from the Na^+ inner shell, while supplementing FSI^- anions to Na^+ clusters at lower temperatures. This solvent-anion exchange agrees with the MD results and results in a faster ionic diffusion as detected by pulsed field gradient 2D diffusion-ordered spectroscopy (DOSY). The 2D DOSY (Figure 2e,f) at −20 °C shows that self-diffusion coefficients (D) of both DME (7.94×10^{-12} m^2 s^{-1}) and FSI anions (6.8×10^{-12} m^2 s^{-1}) in LHCE_0.3IL are slightly larger than that in bare LHCE. The mean squared distance derived from MD simulation also demonstrates that LHCE_0.3IL has higher Na^+ diffusivity than bare LHCE (Figure S14, Supporting Information). Thus, our results demonstrate that, unlike the non-solvating diluent, C_3mpyrFSI IL acts as a special diluent to play a critical role, in enhancing $Na^+\cdots FSI^-$ionic pairs and decreasing $Na^+\cdots$DME ionic-dipole pairs via anion-solvent exchange. This is of significance to the interfacial kinetics as revealed below.

The voltage profiles of Na | Na symmetric cells with both electrolytes suggest a consistent Na deposition/stripping throughout the test (**Figure 3**a). However, a notably high overpotential of 0.15 V, with a sharp increase toward the end of the polarization step, was observed in the LHCE system at 1 mA cm^{-1} (Figure S15, Supporting Information). The low overpotential of LHCE_0.3IL partially results from the higher ionic transport, which has also been observed in a previous report.[48] Meanwhile, the contribution of interfacial kinetics to cycling performance will be discussed below. Moreover, although the state-of-the-art LHCE exhibits a decent average CE of 98.1%, the LHCE_0.3IL further upgrades the Cu | Na cell with a significantly higher average CE of 99.3% and a lower overpotential (Figure 3b), which ranks among the highest for Na-metal batteries. Particularly, when cycled at −20 °C, a stable polarization curve was observed over 450 h of cycling in LHCE_0.3IL (Figure 3c), which is unattainable in bare LHCE at −20 °C (Figure S16, Supporting Information). This failure of bare LHCE is also consistent with EIS divergence at −20 °C, where the cell impedance reached as high as 3500 Ω after 50 cycles in a Na | Na cell, whereas the impedance was halved upon the C_3mPyrFSI was applied (Figure 3f).

Energy barriers of Na^+ transport at the interphase were quantified, with the assumption that each transport step is a thermally activated process. The temperature-dependent EIS of the Na | Na symmetric cell consists of two overlapping semicircles (Figure S17, Supporting Information), which represent the impedance

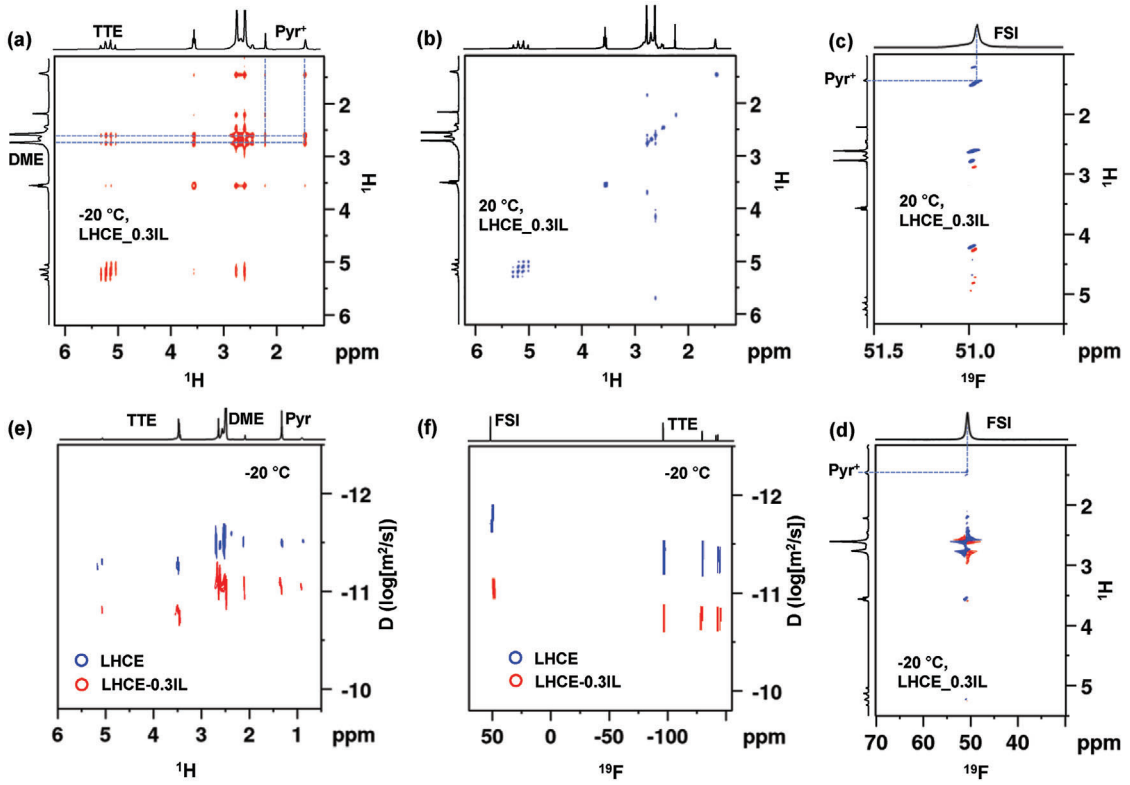

Figure 2. Nanostructured arrangement of electrolytes analyzed by 2D NMR. ^{1}H-^{1}H HOESY NMR spectra of LHCE_0.3IL at a) 20 °C and b) −20 °C. c, d) ^{1}H-^{19}F HOESY spectra of LHCE_0.3IL at 20 and −20 °C. e) 2D DOSY of ^{1}H NMR for LHCE and LHCE_0.3IL at −20 °C. f) 2D DOSY spectra of ^{19}F NMR for the electrolytes at −20 °C.

of Na transport through the SEI film (R_{SEI}) and Na^+ de-solvation process (R_{ct}). Thus, the activation energy for Na^+ de-solvation ($E_{a,\ ct}$) and its diffusion through SEI ($E_{a,\ SEI}$) can be obtained according to the Arrhenius equation (Figure S17, Supporting Information). As shown in Figure 3d, the $E_{a,\ SEI}$ in the LHCE-0.3IL electrolyte is calculated to be 45.2 kJ mol^{-1}, much lower than the 59.2 kJ mol^{-1} for the traditional LHCE electrolyte. Meanwhile, the Na^+-desolvation energy barrier is further decreased to 49.4 kJ mol^{-1} (60 kJ mol^{-1} for LHCE electrolyte, Figure 3e). The lower desolvation barrier can be rationalized because of the loose $Na^{+\cdots}$DME coordination in LHCE_0.3IL at −20 °C (as revealed by NMR and MD simulation), which facilitates the most rate-determining step (desolvation process) during Na^+ deposition. Additionally, the lower $E_{a,\ SEI}$ is related to interfacial structure which is further disclosed below.

Since interfacial kinetics is relatively not the limiting factor at room or high temperatures, LHCE generally enables a compact metal deposition. However, if the temperature is reduced to −20 °C, the interfacial resistance for LHCE electrolyte is above 2 times that of LHCE-0.3IL as shown in Figure S17 (Supporting Information). This means favorable interfacial kinetics enabled by LHCE_0.3IL plays an important role in decreasing the overpotential, which is critical to regulating the Na deposition behavior.[49] The correlation between the critical nuclei radius and the nucleation overpotential can be evaluated by the equation:[50,51] $r = 2\gamma V_m/(F|\eta_n|)$, where r and γ are the radius of the nucleus and the surface energy of Na/electrolyte interface, respectively. V_m refers to the molar volume of Na, F is the Faraday's constant, and η_n is the nucleation overpotential. Therefore, the much lower interfacial resistance obtained with IL-assisted LHCE facilitates denser and larger Na deposition at −20 °C, as observed in Figure 3i,j, which points out the importance of interfacial kinetics control toward stabilized Na-metal anodes. By contrast, small and loosely connected Na electrodeposits were observed with a focused ion beam scanning electron microscopy (FIB-SEM, Figure 3g,h).

Interfacial kinetics is highly associated with SEI. The composition and structure were resolved by X-ray photoelectron microscopy (XPS) depth profiling and time-of-flight secondary ion mass spectrometry (ToF-SIMS). As shown in Figure 4a, the C/C-O XPS contour mapping reveals that the SEI in LHCE (−20 °C) contains substantial organic components, while they are almost invisible in the LHCE_0.3IL based SEI at both 20 °C and −20 °C. On the contrary, The NaF signals representing the inorganic species are much more prominent in the contour mapping (Figure 4b). After 10 min of sputtering, the electrodeposits in LHCE-0.3IL show an F/C atomic ratio over 100 times higher and a much stronger Na_2S/S2p ratio (Figure 4c,d), validating the dominance of an inorganic interphase. This inorganic interphase results in robust mechanical properties, as revealed by atomic force microscopy in Figure S18 (Supporting Information). The 3D rendering space in ToF-SIMS further visualized the significantly suppressed solvent decomposition in IL-assisted LHCE regardless of the decreased temperature, as disclosed by the much weaker C_2HO^- 3D rendering space over the whole investigated

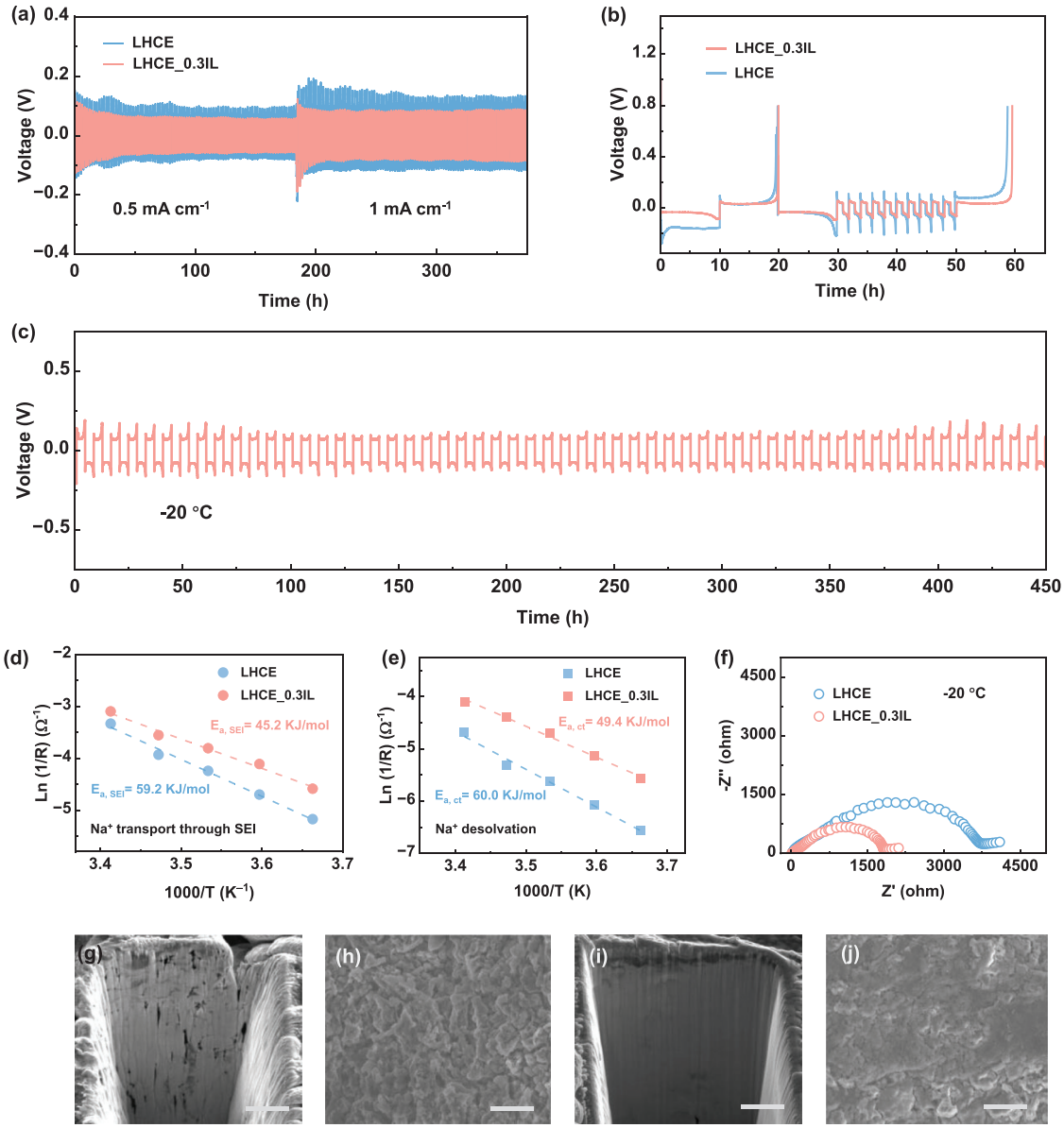

Figure 3. a) Voltage profiles of the Na | Na symmetric cells with electrolytes at 20 °C. b) Average CE measurements of Na-Cu cells at 0.5 mA cm^{-2}. c) Voltage profiles of the Na | Na symmetric cells with LHCE_0.3IL at −20 °C and 0.2 mA × 4 h. Activation energies of d) charge transfer and e) Na-ion transport through interphase. f) Nyquist plots of the Na | Na cells at −20 °C with LHCE and LHCE_0.3IL electrolytes after 50 cycles. FIB-SEM and SEM images of Na deposits at −20 °C in g,h) LHCE and i,j) LHCE_0.3IL. The scale bar is 5 µm.

depth (Figure 4h,i). By contrast, Figure 4g illustrates that LHCE results in organic and thick interphase at −20 °C, rather than the previously observed inorganic SEI formed at room temperature. The diminished Na^- spatial occupation and high C_2HO^- signal at the top 10 nm are observed in LHCE-based SEI at −20 °C (Figure 4e,f). This indicates substantial corrosion of active Na^0 on the surface instead of its involvement in SEI formation. Conversely, IL-assisted LHCE leads to a more uniform interface with notable anion salt decomposition products including SN^- even at −20 °C (Figure 4i). These findings clearly show that the traditional LHCE formed a compromised interface at low temperatures, but the IL helps reconstruct the interface with compact and inorganic structures at −20 °C and consequently offers a lower $E_{a,SEI}$.

The upgraded ionic dynamics at both the bulk solution and Na interface contributed to a superior performance of the Na–S cell. Note that sulfurized polyacrylonitrile (SPAN) is used as a cathode here capitalizing on the covalent bonding of sulfur with the polymeric backbone, which can better suppress sulfur dissolution. Nevertheless, the cathode in traditional electrolytes (such as 2 M LiTFSI in DME) still experiences rapid capacity decay (Figure S19, Supporting Information). The Na–SPAN cell in LHCE shows a respectable specific capacity, but the rate performance and long-term stability are far from satisfactory. As

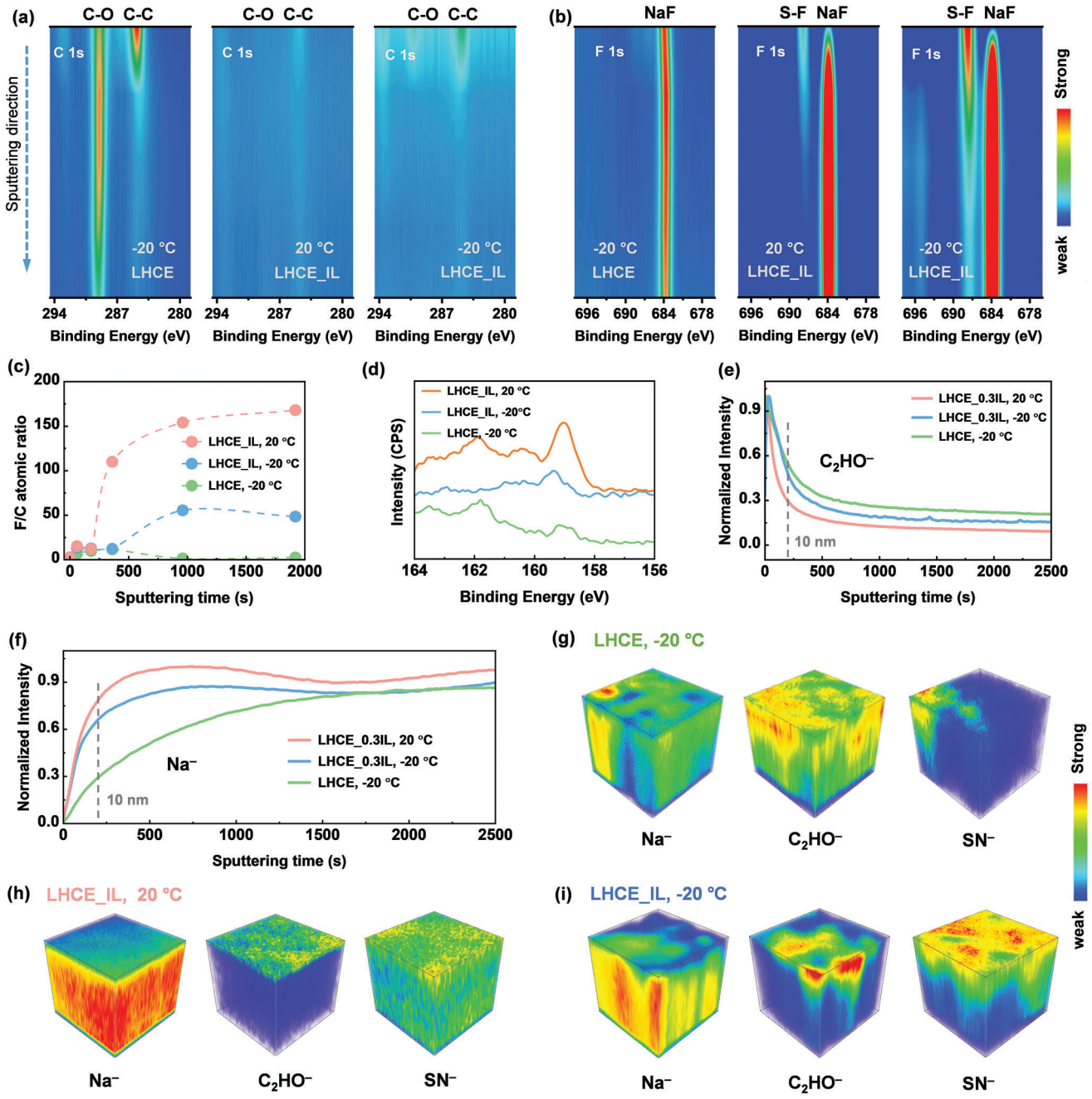

Figure 4. Characterization of the Na anode interphase after 50 cycles. Contour plots of the XPS: a) C1s and b) F1s spectra of the cycled Na-metal anodes at 20 °C and −20 °C with the two electrolytes. c) Atomic intensity ratio of F/C peak and d) S 2p spectra of the SEI after 10 min of sputtering. e, f) Depth profiles of C_2HO^- and Na^- signals collected from the cycled Na anodes. g–i) 3D rendering of ToF-SIMS secondary-ion fragments sputtered from the cycled Na anodes. C_2HO^- species result from solvents decomposition; the NaF_2^- and SN^- fragments are from FSI^- anion decomposition.

depicted in **Figure** 5a, capacities below 0.5C rate are comparable for both electrolytes, yet the LHCE cell jumps quickly to ≈400 mAh g^{-1} at a 3C rate. In contrast, the LHCE_0.3IL cell delivers capacities of 640, 601, and 573 mAh g^{-1} at, respectively, 1, 2, and 3C rates (Figure 5b), and can fully restore the initial capacity at 0.5C rate without decay over the next 100 cycles. Long-term cycling over 250 cycles at a 1C rate demonstrates 95% capacity retention (Figure S20, Supporting Information). Particularly notable is the exceptional performance achieved at low temperatures (Figure 5c,d). The Na–S cells were continuously cycled at 0.2C rate at 10, 0, −10, and −20 °C. At −20 °C, a high capacity of 450 mAh g^{-1} is retained after 200 cycles with an average CE of ≈100% in LHCE_0.3IL. The capacity at −20 °C is ≈73.3% of that at 10 °C, whereas, this ratio sharply decreases to 41.2% for the bare LHCE system (257 mAh g^{-1}), which can be linked to the huge polarization of sodium deposition at a lower

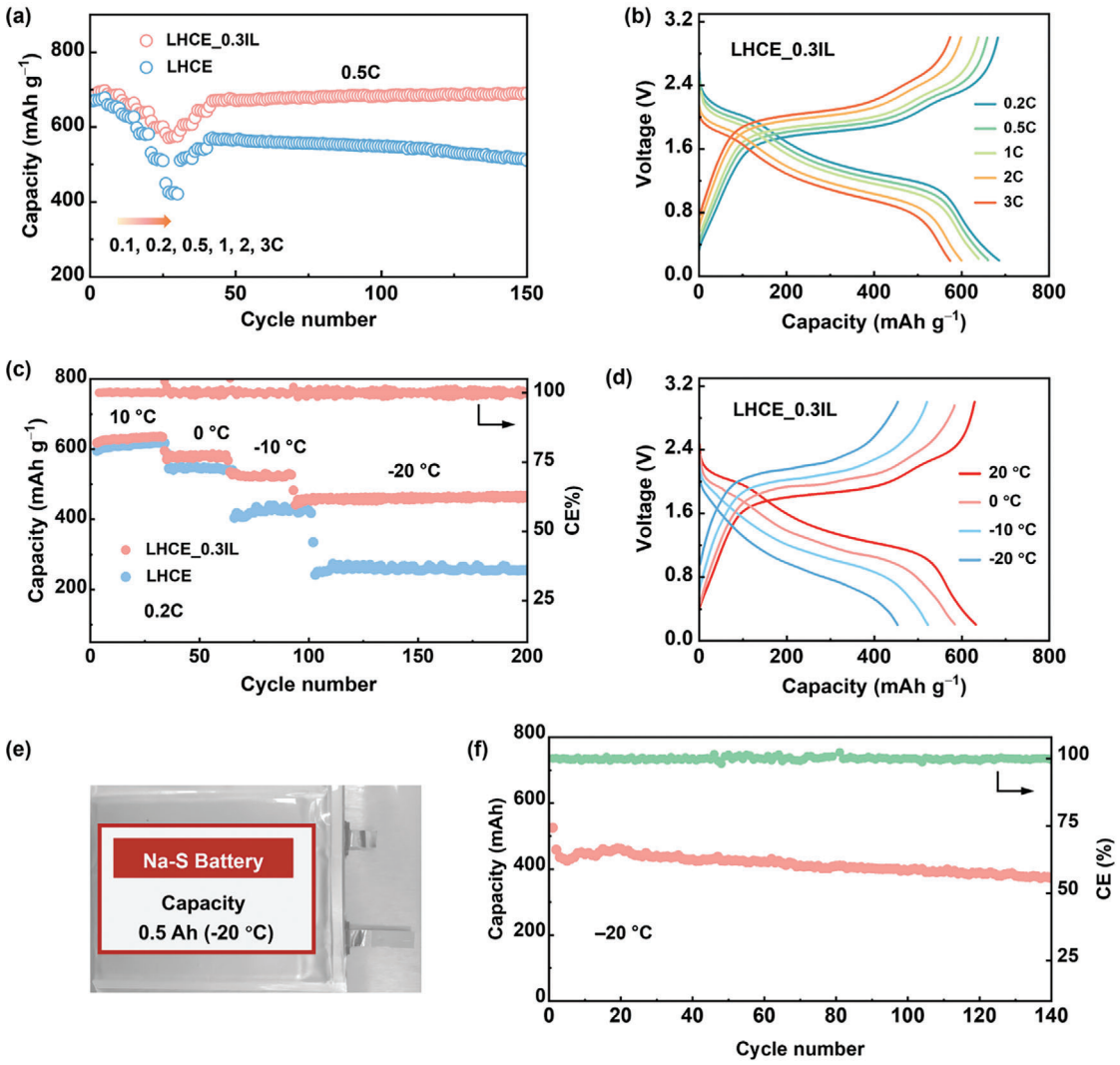

Figure 5. Electrochemical performances of Na–SPAN cells. a) Rate performances and the accompanying long-term cycling performance at 20 °C. b) The corresponding discharge–charge curves at different C rates with LHCE_0.3IL electrolyte. c) Long-term cycling performance at 0.2C rate at low temperatures down to −20 °C, and d) the corresponding voltage profiles with LHCE_0.3IL electrolyte. (e) Photograph of the fabricated Na–SPAN pouch cell. f) Pouch cell performance at −20 °C and 0.1C rate with the LHCE_0.3IL electrolyte.

temperature. To the best of our knowledge, this represents the first report of low-temperature Na–S batteries, and the performance is competitive to other types of low-temperature battery technologies (Table S3, Supporting Information). Moreover, even when tested at −30 °C, the Na–S cell still delivered a capacity of ≈280 mAh g-1 at a 0.1C rate. The cell with LHCE_0.3IL electrolyte can recover the initial capacities at 20 °C after an ultralow-temperature operation at −30 °C (Figure S21, Supporting Information) and exhibit decent rate performance at different temperatures (Figure S22, Supporting Information), further suggesting that the inorganic-rich interphases are durable enough to support low-temperature cycling.

Pouch cells offer more practical scenarios for validating the low-temperature performance. High-loading SPAN cathodes (7.4 mg cm^{-2}, double side) paired with Na metal anodes (200 µm, N/P ratio: ≈5) and lean electrolyte (6 µL mg^{-1}) were employed to assemble a 0.5 Ah pouch cell (Figure 5e). At −20 °C and a 0.1C rate, the initial discharge capacity reaches ≈450 mAh, with a retained capacity of 420 mAh after 50 cycles, corresponding to a retention rate of 93%. After 140 cycles, the pouch cell still maintains a decent capacity of 372 mAh (82% capacity retention). The sodium metal anode also shows a robust interphase after cycling in the pouch cell (Figure S23, Supporting Information). Moreover, the energy density was calculated to be ≈108 Wh kg^{-1} at −20 °C. Even after 100 cycles, an energy density of 95 Wh kg^{-1} can be retained. This energy density and cyclability are competitive compared to the reported state-of-the-art low-temperature battery technologies, such as Na-ion batteries,[52] lithium-metal batteries,[19] and potassium batteries.[53] In this regard, the developed LHCE_0.3IL electrolyte provides a promising strategy for mitigating the sluggish kinetics at low temperatures, which is highly demanding for Na–S batteries working at extreme conditions. While the developed electrolyte demonstrates high safety (Figure S24, Supporting Information) and significantly improved

kinetics, the long-term stability of the low-temperature Na anode requires further enhancement. A promising approach for future research could involve a combination of electrolyte engineering and artificial interphase protection methods, such as alloy engineering (e.g., Na–Sn), polymeric coatings, and Na host engineering.

3. Conclusion

Traditional LHCE is revealed to be ineffective for low-temperature sodium–sulfur batteries. In this work, we identified that ionic liquid could be a critical solvating species in LHCE to stabilize Na–S batteries at low temperatures. A proper amount of C_3mpyrFSI ionic liquid can transform both the meso- and micro-structure of the LHCE. Computational simulation, SAXS, and 2D NMR revealed that in the IL-mediated LHCE, smaller-size clusters are developed, and more FSI^- anions, yet less DME solvents, occupy the Na^+ inner solvation structure due to the solvent-anion exchange between the organic and inorganic cation solvation structures; this finding has not been reported before. The ionic liquid-mediated LHCE electrolyte offers faster Na-ion mobility and a stable Na-metal anode interface at −20 °C, which is critical for the low-temperature operation of sodium–sulfur batteries under practical conditions. The LHCE_0.3IL further pushes the limit of traditional LHCE, and this new electrolyte tailoring strategy opens a new direction for other extreme batteries with high-voltage, fast-charging, or wide-temperature scenarios.

Supporting Information

Supporting Information is available from the Wiley Online Library or from the author.

Acknowledgements

This work was supported by the U.S. Department of Energy, Office of Basic Energy Sciences, Division of Materials Sciences and Engineering under award number DE-SC0005397. Computational calculation work supported by the Welch Foundation grant F-1841 and the National Energy Scientific Research Center and ACCESS Anvil supercomputer at Purdue University.

Conflict of Interest

The authors declare no conflict of interest.

Data Availability Statement

The data that support the findings of this study are available from the corresponding author upon reasonable request.

Keywords

electrolyte engineering, ionic liquid, low-temperature batteries, sodium metal batteries, sodium–sulfur batteries

Received: July 2, 2024
Revised: September 15, 2024
Published online: October 8, 2024

[1] Z. Shi, Z. Tian, D. Guo, Y. Wang, Z. Bayhan, A. S. Alzahrani, H. N. Alshareef, *ACS Energy Lett.* **2023**, *8*, 3054.
[2] A. Manthiram, Y. Fu, S. H. Chung, C. Zu, Y. S. Su, *Chem. Rev.* **2014**, *114*, 11751.
[3] D. Guo, X. Li, W. Wahyudi, C. Li, A.-H. Emwas, M. N. Hedhili, Y. Li, Z. Lai, *ACS Nano.* **2020**, *14*, 17163.
[4] D. Guo, M. Li, M. N. Hedhili, V. Tung, Y. Li, Z. Lai, *Energy Storage Mater.* **2019**, *25*, 33.
[5] Z. Shi, S. Thomas, Z. Tian, D. Guo, Z. Zhao, Y. Wang, S. Li, N. Wehbe, A.-H. Emwas, O. M. Bakr, O. F. Mohammed, H. N. Alshareef, *Nano Research Energy.* **2024**, *3*, 9120126.
[6] S. Tang, Q. Chen, Y. Si, W. Guo, B. Mao, Y. Fu, *Adv. Mater.* **2021**, *33*, 2100824.
[7] Z. Tian, Y. Zou, G. Liu, Y. Wang, J. Yin, J. Ming, H. N. Alshareef, *Adv. Sci.* **2022**, *9*, 2201207.
[8] L. Lin, C. Zhang, Y. Huang, Y. Zhuang, M. Fan, J. Lin, L. Wang, Q. Xie, D. L. Peng, *Small.* **2022**, *18*, 2107368.
[9] X. Zheng, L. Huang, X. Ye, J. Zhang, F. Min, W. Luo, Y. Huang, *Chem.* **2021**, *7*, 2312.
[10] B. Lee, E. Paek, D. Mitlin, S. W. Lee, *Chem. Rev.* **2019**, *119*, 5416.
[11] Y. Chen, Z. Yu, P. Rudnicki, H. Gong, Z. Huang, S. C. Kim, J. C. Lai, X. Kong, J. Qin, Y. Cui, Z. Bao, *J. Am. Chem. Soc.* **2021**, *143*, 18703.
[12] Y. Zhao, T. Zhou, T. Ashirov, M. E. Kazzi, C. Cancellieri, L. P. H. Jeurgens, J. W. Choi, A. Coskun, *Nat. Commun.* **2022**, *13*, 2575.
[13] Y. Jin, P. M. L. Le, P. Gao, Y. Xu, B. Xiao, M. H. Engelhard, X. Cao, T. D. Vo, J. Hu, L. Zhong, B. E. Matthews, R. Yi, C. Wang, X. Li, J. Liu, J.-G. Zhang, *Nat. Energy.* **2022**, *7*, 718.
[14] Q.-K. Zhang, X.-Q. Zhang, J. Wan, N. Yao, T.-L. Song, J. Xie, L.-P. Hou, M.-Y. Zhou, X. Chen, B.-Q. Li, R. Wen, H.-J. Peng, Q. Zhang, J.-Q. Huang, *Nat. Energy.* **2023**, *8*, 725.
[15] Q. Wang, C. Zhao, J. Wang, Z. Yao, S. Wang, S. G. H. Kumar, S. Ganapathy, S. Eustace, X. Bai, B. Li, M. Wagemaker, *Nat. Commun.* **2023**, *14*, 440.
[16] S. H. Lee, J. Y. Hwang, J. Ming, Z. Cao, H. A. Nguyen, H. G. Jung, J. Kim, Y. K. Sun, *Adv. Energy. Mater.* **2020**, *10*, 2000567.
[17] S. Tan, Z. Shadike, X. Cai, R. Lin, A. Kludze, O. Borodin, B. L. Lucht, C. Wang, E. Hu, K. Xu, X.-Q. Yang, *Electrochem. Energy Rev.* **2023**, *6*, 35.
[18] X. Zhang, Z. Cui, A. Manthiram, *Adv. Funct. Mater.* **2023**, 2309591.
[19] J. Holoubek, H. Liu, Z. Wu, Y. Yin, X. Xing, G. Cai, S. Yu, H. Zhou, T. A. Pascal, Z. Chen, P. Liu, *Nat. Energy.* **2021**, *6*, 303.
[20] L. Hu, J. Deng, Y. Lin, Q. Liang, B. Ge, Q. Weng, Y. Bai, Y. Li, Y. Deng, G. Chen, X. Yu, *Adv. Mater.* **2024**, 2312161.
[21] S. Wang, X. G. Zhang, Y. Gu, S. Tang, Y. Fu, *J. Am. Chem. Soc.* **2024**, *146*, 3854.
[22] V. Kumar, A. Y. S. Eng, Y. Wang, D.-T. Nguyen, M.-F. Ng, Z. W. Seh, *Energy Storage Mater.* **2020**, *29*, 1.
[23] J. Wu, J. Liu, Z. Lu, K. Lin, Y.-Q. Lyu, B. Li, F. Ciucci, J.-K. Kim, *Energy Storage Mater.* **2019**, *23*, 8.
[24] J. He, A. Bhargav, W. Shin, A. Manthiram, *J. Am. Chem. Soc.* **2021**, *143*, 20241.
[25] Z. Yan, J. Xiao, W. Lai, L. Wang, F. Gebert, Y. Wang, Q. Gu, H. Liu, S. L. Chou, H. Liu, S. X. Dou, *Nat. Commun.* **2019**, *10*, 4793.
[26] Y. Ren, T. Lai, A. Manthiram, *ACS Energy Lett.* **2023**, *8*, 2746.
[27] D. Guo, F. Ming, H. Su, Y. Wu, W. Wahyudi, M. Li, M. N. Hedhili, G. Sheng, L.-J. Li, H. N. Alshareef, Y. Li, Z. Lai, *Nano Energy.* **2019**, *61*, 478.
[28] D. Guo, X. Li, F. Ming, Z. Zhou, H. Liu, M. N. Hedhili, V. Tung, H. N. Alshareef, Y. Li, Z. Lai, *Nano Energy.* **2020**, *73*, 104769.
[29] X. Ren, S. Chen, H. Lee, D. Mei, M. H. Engelhard, S. D. Burton, W. Zhao, J. Zheng, Q. Li, M. S. Ding, M. Schroeder, J. Alvarado, K. Xu, Y. S. Meng, J. Liu, J.-G. Zhang, W. Xu, *Chem.* **2018**, *4*, 1877.
[30] D. Guo, J. Wang, T. Lai, G. Henkelman, A. Manthiram, *Adv. Mater.* **2023**, *35*, 2300841.

[31] C. M. Efaw, Q. Wu, N. Gao, Y. Zhang, H. Zhu, K. Gering, M. F. Hurley, H. Xiong, E. Hu, X. Cao, W. Xu, J. G. Zhang, E. J. Dufek, J. Xiao, X. Q. Yang, J. Liu, Y. Qi, B. Li, *Nat. Mater.* **2023**, *22*, 1531.
[32] Y. Yamada, J. Wang, S. Ko, E. Watanabe, A. Yamada, *Nat. Energy.* **2019**, *4*, 269.
[33] X. Zheng, Z. Gu, J. Fu, H. Wang, X. Ye, L. Huang, X. Liu, X. Wu, W. Luo, Y. Huang, *Energy Environ. Sci.* **2021**, *14*, 4936.
[34] C. Wang, A. C. Thenuwara, J. Luo, P. P. Shetty, M. T. McDowell, H. Zhu, S. Posada-Perez, H. Xiong, G. Hautier, W. Li, *Nat. Commun.* **2022**, *13*, 4934.
[35] C. Yang, X. Liu, Y. Lin, L. Yin, J. Lu, Y. You, *Adv. Mater.* **2023**, *35*, 2301817.
[36] X. Zheng, Z. Cao, W. Luo, S. Weng, X. Zhang, D. Wang, Z. Zhu, H. Du, X. Wang, L. Qie, H. Zheng, Y. Huang, *Adv. Mater.* **2022**, *35*, 2210115.
[37] B. Nan, L. Chen, N. D. Rodrigo, O. Borodin, N. Piao, J. Xia, T. Pollard, S. Hou, J. Zhang, X. Ji, J. Xu, X. Zhang, L. Ma, X. He, S. Liu, H. Wan, E. Hu, W. Zhang, K. Xu, X. Q. Yang, B. Lucht, C. Wang, *Angew. Chem., Int. Ed.* **2022**, *61*, 202205967.
[38] N. Zhang, T. Deng, S. Zhang, C. Wang, L. Chen, C. Wang, X. Fan, *Adv. Mater.* **2022**, *34*, 2107899.
[39] G. Zhang, J. Chang, L. Wang, J. Li, C. Wang, R. Wang, G. Shi, K. Yu, W. Huang, H. Zheng, T. Wu, Y. Deng, J. Lu, *Nat. Commun.* **2023**, *14*, 1081.
[40] J. Xu, J. Zhang, T. P. Pollard, Q. Li, S. Tan, S. Hou, H. Wan, F. Chen, H. He, E. Hu, K. Xu, X. Q. Yang, O. Borodin, C. Wang, *Nature.* **2023**, *614*, 694.
[41] F. Wu, S. Fang, M. Kuenzel, A. Mullaliu, J.-K. Kim, X. Gao, T. Diemant, G.-T. Kim, S. Passerini, *Joule.* **2021**, *5*, 2177.
[42] X. Wang, F. Chen, G. M. A. Girard, H. Zhu, D. R. MacFarlane, D. Mecerreyes, M. Armand, P. C. Howlett, M. Forsyth, *Joule.* **2019**, *3*, 2687.
[43] P. Nurnberg, J. Atik, O. Borodin, M. Winter, E. Paillard, M. Schonhoff, *J. Am. Chem. Soc.* **2022**, *144*, 4657.
[44] H. K. Bergstrom, B. D. McCloskey, *ACS Energy Lett.* **2024**, *9*, 373.
[45] S. C. Kim, J. Wang, R. Xu, P. Zhang, Y. Chen, Z. Huang, Y. Yang, Z. Yu, S. T. Oyakhire, W. Zhang, L. C. Greenburg, M. S. Kim, D. T. Boyle, P. Sayavong, Y. Ye, J. Qin, Z. Bao, Y. Cui, *Nat. Energy.* **2023**, *8*, 814.
[46] K. Qian, R. E. Winans, T. Li, *Adv. Energy Mater.* **2020**, *11*, 2002821.
[47] D. Guo, D. B. Shinde, W. Shin, E. Abou-Hamad, A. H. Emwas, Z. Lai, A. Manthiram, *Adv. Mater.* **2022**, *34*, 2201410.
[48] U. Pal, D. Rakov, B. Lu, B. Sayahpour, F. Chen, B. Roy, D. R. MacFarlane, M. Armand, P. C. Howlett, Y. S. Meng, M. Forsyth, *Energy Environ. Sci.* **2022**, *15*, 1907.
[49] X. Gao, Y.-N. Zhou, D. Han, J. Zhou, D. Zhou, W. Tang, J. B. Goodenough, *Joule.* **2020**, *4*, 1864.
[50] D. R. Ely, R. E. García, *J. Electrochem. Soc.* **2013**, *160*, A662.
[51] J. Wang, W. Huang, A. Pei, Y. Li, F. Shi, X. Yu, Y. Cui, *Nat. Energy.* **2019**, *4*, 664.
[52] Q. Zhu, D. Yu, J. Chen, L. Cheng, M. Tang, Y. Wang, Y. Li, J. Yang, H. Wang, *Joule.* **2024**, *8*, 482.
[53] M. Tang, S. Dong, J. Wang, L. Cheng, Q. Zhu, Y. Li, X. Yang, L. Guo, H. Wang, *Nat. Commun.* **2023**, *14*, 6006.